Solitary water waves created by variations in bathymetry

Manuel Quezada de Luna [*]   David I. Ketcheson [†]

July 17, 2019

Abstract

We study water waves in a channel with non-uniform bathymetry including deeper and shallower regions. Propagation of a plane wave in such a channel is equivalent to propagation in a larger periodic domain, and analysis of a linearized, homogenized model shows that wave propagation in this setting is dispersive. Numerical simulations reveal that a balance between this dispersion and the inherent nonlinearity of water waves can create solitary waves. These solitary waves behave similarly to solitary waves that arise in higher-order dispersive wave equations, but can arise in a much more strongly nonlinear regime. Computational experiments using depth-averaged water wave models, as well as the three-dimensional incompressible Navier-Stokes equations for two phase (water-air) immiscible viscous flows, suggest that experimental observation of these solitary waves may be possible.

1   Introduction

There exist many mathematical models for water waves, each applicable in some regime depending on the physical parameters of the waves of interest. Effects that may be important or negligible include nonlinearity, dispersion, viscosity, and surface tension. In regimes where both nonlinearity and dispersion are important, such as that modeled by the Korteweg-de Vries (KdV) equation, solitary waves may arise through a balance of these two effects. In regimes where nonlinearity is dominant, such as that modeled by the shallow water equations, solutions are characterized by wave breaking. These regimes differ markedly from both a mathematical and a physical perspective. In this work, by considering the effects of varying bathymetry, we demonstrate the formation of solitary waves in regimes that would be characterized by wave breaking if there was no bathymetric variation. These solitary waves appear even when solving the shallow water equations, which completely neglect wave dispersion.

Our main object of study is the propagation of a plane wave in a channel where one side is deep and the other shallow. This channel is depicted in Figure 1a. Specifically, the channel extends infinitely

---

[*]KAUST CEMSE, manuel.quezada@kaust.edu.sa.

[†]KAUST CEMSE, david.ketcheson@kaust.edu.sa.

in x and from $-\Omega/4$ to $\Omega/4$ in y, with the bottom height given by

$$b(x,y) = \begin{cases} b_A & y < 0 \\ b_B & y \geq 0. \end{cases} \tag{1}$$

As explained in §2.1, under appropriate boundary and initial conditions this channel can be viewed as part of an infinite periodic domain; see Figure 2. Waves in periodic materials are known to exhibit dispersive effects [21], and dispersion of acoustic waves in a similar domain has been studied in detail in [4, 19] where it was seen as a result of wave diffraction. The solitary water waves that we observe are thus related to the solitary waves observed in [12] as solutions of a two-dimensional p-system with periodically-varying coefficients (so-called *diffractons*).

(a) Channel with layered sections
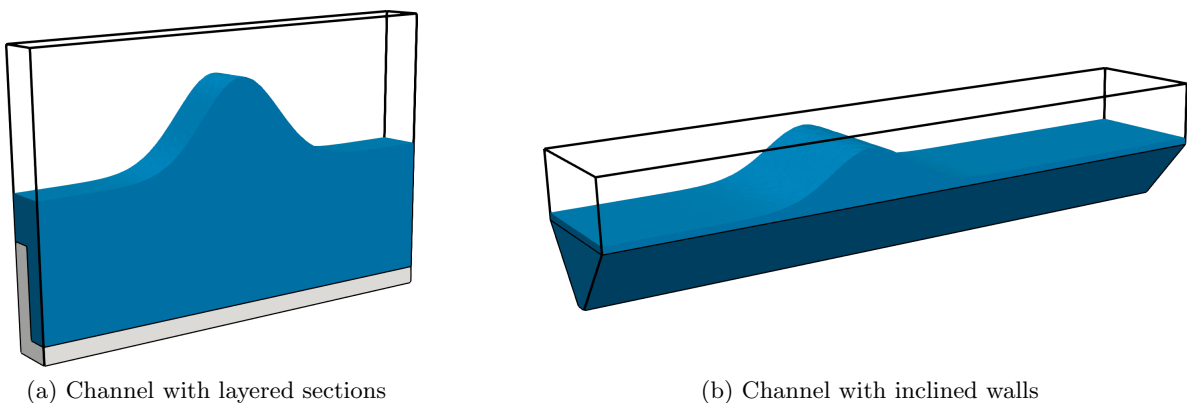
(b) Channel with inclined walls

Figure 1: Bathymetric configurations studied in this work.

The main results of this work are split into four sections. In §2 we consider the (dispersionless) shallow water equations with periodic bathymetry and perform a linearization to show via homogenization that the bathymetry variation introduces an effective dispersion for small-amplitude waves. In §3 we perform numerical simulations of the shallow water equations with periodic bathymetry and obtain solitary waves. We also compare some properties of these solitary waves with those of the diffractons observed in [12]. Following [12], we refer to these solitary waves as shallow water diffractons, or SW diffractons. The shallow water model neglects important physical effects such as dissipation, surface tension and dispersion. These processes might be important for this particular problem. As a result, a natural question arises: can these waves be observed in a physical experiment? In §4 we address this question by considering two regimes where SW diffractons are formed. The first regime is weakly nonlinear, and in this regime water waves undergo significant dispersion even over flat bathymetry; see e.g. [13]. We consider the Korteweg-de Vries (KdV) equation, which models shallow and weakly nonlinear water waves over flat bathymetry, and is known to have soliton solutions. We compare KdV solitons with SW diffractons. The second regime we study is more strongly nonlinear; here the KdV equation is not valid. Instead, we consider the three dimensional Navier-Stokes equations for

two-phase incompressible viscous flows and solve them numerically for flat and periodic bathymetry profiles. Again we observe solitary waves, which we call *water-wave diffractons*. We compare these waves with the SW diffractons. Finally, in §5 we consider a more natural channel with inclined walls, like the one shown in Figure 1b. Again we obtain SW diffractons, which suggests that SW and water-wave diffractons might arise under a range of bathymetric profiles. We close this work in §6 with some conclusions and discussion.

The code and instructions to create every figure and all the results in this work is available at https://github.com/manuel-quezada/water_wave_diffractons_RR.

2 Effective dispersion of waves due to bathymetry

In this section we show that waves in a channel with varying bathymetry undergo dispersion. The explanation for this relies on an equivalence between the channel and an infinite periodic domain, which we describe first.

2.1 The channel as part of a periodic domain

In this work we study flow in a channel as described above, with $x \in [0, \infty)$, $y \in [-\Omega/4, \Omega/4]$, bathymetry given by (1), and with initial data that varies only with x. The boundary conditions at the sides of the channel are taken as reflecting for the normal component of velocity and slip for the tangential component of velocity.

In this section we also consider a different domain, extending infinitely in both x and y, with bathymetry periodic in y. Specifically, let $y^* = y/\Omega$ and let

$$b(x,y) = \begin{cases} b_A & \text{if } n + \frac{1}{2} \leq y^* \leq n + 1 \\ b_B & \text{if } n \leq y^* \leq n + \frac{1}{2}. \end{cases} \tag{2}$$

Here n is any integer. Again let the initial data vary only with x. Then because of symmetry, the solution must have the property that the y-component of velocity vanishes along each line $y = (2n+1)\Omega/4$, $\forall n \in \mathbb{Z}$. In other words, the solution of this second problem satisfies exactly the boundary conditions of the first problem. Because of this, the solution of the second problem, restricted to $y \in [-\Omega/4, \Omega/4]$, is identical to the solution in the channel.

These two domains and their correspondence are depicted in Figure 2. In the remainder of this section we study the effect of the periodic domain in order to draw conclusions about the behavior of the wave in a channel. Although we focus on piecewise-constant bathymetry, similar phenomena appear in computational experiments with other kinds of bathymetry; see §5 and [12].

2.2 Linearization and homogenization

Water waves are inherently dispersive, and this is represented through dispersive terms in models such as the Korteweg-de Vries (KdV) equation [13], the Boussinesq equations [1], and the Green-Naghdi
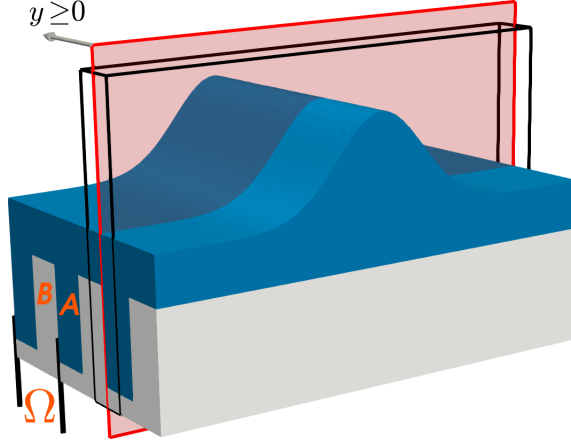
3

Figure 2: Periodic bathymetric configuration studied in this work (see (2)). The outlined (black) box represents the channel in Figure 1a. The red plane represents $y = 0$.

model [6]. In this section, we demonstrate that small-amplitude shallow water waves propagating over periodic bathymetry undergo an effective dispersion. In order to clearly distinguish this source of dispersion from the dispersion present over flat bathymetry, we focus on the –dispersionless– shallow water equations [3]. The analysis and results of this section are similar to those presented in [19], which treated the acoustic wave equation in a periodic medium.

The shallow water equations over variable bathymetry are given by

$$h_t + (hu)_x + (hv)_y = 0, \tag{3a}$$

$$(hu)_t + (hu^2 + gh^2/2)_x + (huv)_y = -ghb_x, \tag{3b}$$

$$(hv)_t + (huv)_x + (hv^2 + gh^2/2)_y = -ghb_y, \tag{3c}$$

where h is the water depth, u and v are the x- and y-velocities respectively, g is the magnitude of the gravitational force and $b(x, y)$ is the periodic bathymetry, see Figure 3. Unless otherwise noted, we use $g = 9.8 \left(\frac{m}{s^2}\right)$; hereafter, we will not explicitly reference units of measure but use SI units throughout. The shallow water model (3) is a first-order hyperbolic system and as such is non-dispersive.

We aim to obtain a constant-coefficient homogenized system that approximates (3) for small-amplitude, long-wavelength perturbations. Let $\eta = h + b$ denote the surface elevation and $\mu = hu$ and $\nu = hv$ denote the x- and y-momentum, respectively. We consider small-amplitude waves with $\eta = \eta_0 + \mathcal{O}(\epsilon)$, $\mu = \mathcal{O}(\epsilon), \nu = \mathcal{O}(\epsilon)$ where $\epsilon \ll 1$ and perform an asymptotic expansion around $\eta = \eta_0$, $\mu = 0$ and $\nu = 0$. The leading-order system is

$$\eta_t + \mu_x + \nu_y = 0, \tag{4a}$$

$$\mu_t + g(\eta_0 - b(x, y))\eta_x = 0, \tag{4b}$$

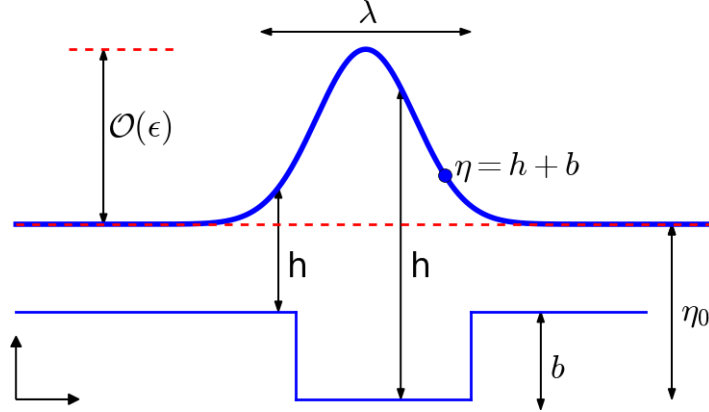$$\nu_t + g(\eta_0 - b(x, y))\eta_y = 0. \tag{4c}$$

4

Figure 3: Notation for shallow water equations with variable bathymetry.

We have explicitly noted the spatial dependence of the bathymetry b in order to emphasize that (4) is a first-order linear hyperbolic system with spatially-varying coefficients. To gain more insight into the behavior of (4), we approximate it via a constant-coefficient system with additional terms. To do this we consider waves with characteristic wavelength λ propagating over a typical distance L in the presence of periodic bathymetry with period Ω, where $\Omega \ll \lambda \ll L$. The homogenized system is derived via a perturbation expansion using $\delta = \Omega/\lambda$ as small parameter and by introducing a fast scale $\hat{y} = \delta^{-1}y$. We consider a plane wave that does not vary (on the macroscopic scale) in the y direction. By using a process very similar to that described in [19] and references therein, we obtain the one-dimensional homogenized model

$$\eta_t + \mu_x = 0, \tag{5a}$$
$$\mu_t + g\langle\eta_0 - b\rangle\eta_x = -g\langle\eta_0 - b\rangle\alpha\eta_{xxx}. \tag{5b}$$

where $\langle f \rangle = \frac{1}{\Omega} \int_{-\Omega/2}^{\Omega/2} f(\hat{y})d\hat{y}$ denotes the average of f over one period of the bathymetry b. The speed of small-amplitude, long wavelength perturbations is $c_{\text{eff}} = \sqrt{g\langle\eta_0 - b\rangle}$. The term appearing on the right hand side of (5) is dispersive; the coefficient of dispersion is given by

$$\alpha = \frac{(b_A - b_B)^2\Omega^2}{192(\eta_0 - b_A)(\eta_0 - b_B)}.$$

It is evident that this dispersion is purely an effect of the bathymetric variation; notice that it increases as the difference between b_A and b_B grows and vanishes as $\eta_0 \to \infty$ (keeping the bathymetry fixed).

In Figure 4 we compare the solution of the (nonlinear) shallow water system with variable bathymetry (3) to that of the homogenized linear system (5). We take initial data

$$\eta(x, y, t = 0) = \eta_0 + \epsilon \exp\left(-\frac{x^2}{2\sigma^2}\right), \qquad u(x, y, 0) = v(x, y, 0) = 0 \tag{6}$$

with $\epsilon = 0.001, \sigma^2 = 2$ and $\eta_0 = 0.75$. The bathymetry is given by (2) with

$$b_A = 0 \qquad b_B = 0.5. \tag{7}$$

The dispersion predicted by the linearized, homogenized model is also clearly evident in the nonlinear, variable-coefficient solution. Both models are solved to very high precision; the differences between the solutions are primarily due to the nonlinear effects that are neglected in (5).
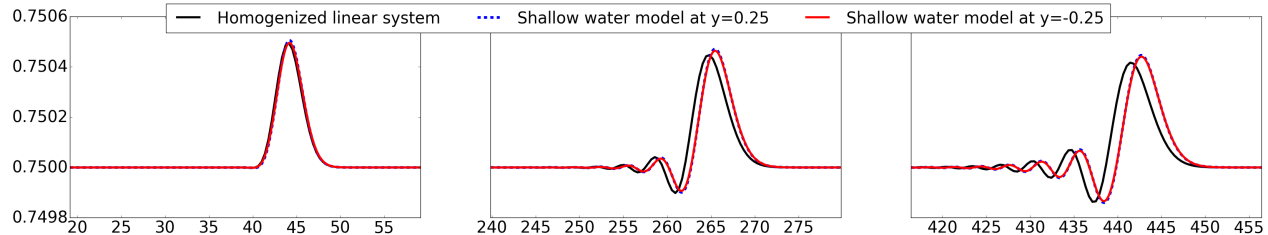

Figure 4: Comparison of a solution of the full shallow water equations (3) with periodic bathymetry versus a solution of the linearized homogenized approximation (5). We show the solution at $t = 20,\ 120$ and $t = 200$.

Remark 2.2.1 (About the numerical methods). *The shallow water equations (3) with variable bathymetry are solved using the finite volume code PyClaw [11], with the Riemann solver developed in [5]. The mesh resolution is $\Delta x = \Delta y = 1/128$. The linear homogenized equations (5) are solved using a Fourier spectral collocation method in space and a fourth order Runge-Kutta method in time; see [23].*

3 Shallow-Water diffractons

Let us now study solutions of the nonlinear, variable-coefficient shallow water model (3) in a more strongly nonlinear regime. We repeat the experiment above, taking (6) and (7) but with a much larger perturbation given by $\epsilon = 0.05$ and $\sigma^2 = 2$ or $\sigma^2 = 10$. We again use the finite volume solver PyClaw, as explained in remark 2.2.1. The results are shown in Figure 5. The mass of the initial pulse determines the number of SW diffractons created. In the rest of this section we use the SW diffractons shown in Figure 5 and (following [12]) study some properties for these solitary waves. In particular, we investigate the long-time stability and shape evolution, the speed-amplitude and scaling relations and the interaction of SW diffractons.

3.1 Long-time stability and shape evolution

We first investigate the long-time behavior and the shape evolution of SW diffractons. To do this we isolate the first solitary wave in Figure 5a and propagate it by itself to $t = 100$. Let $X(t)$ denote the

(a) Initial Gaussian pulse with variance of 2

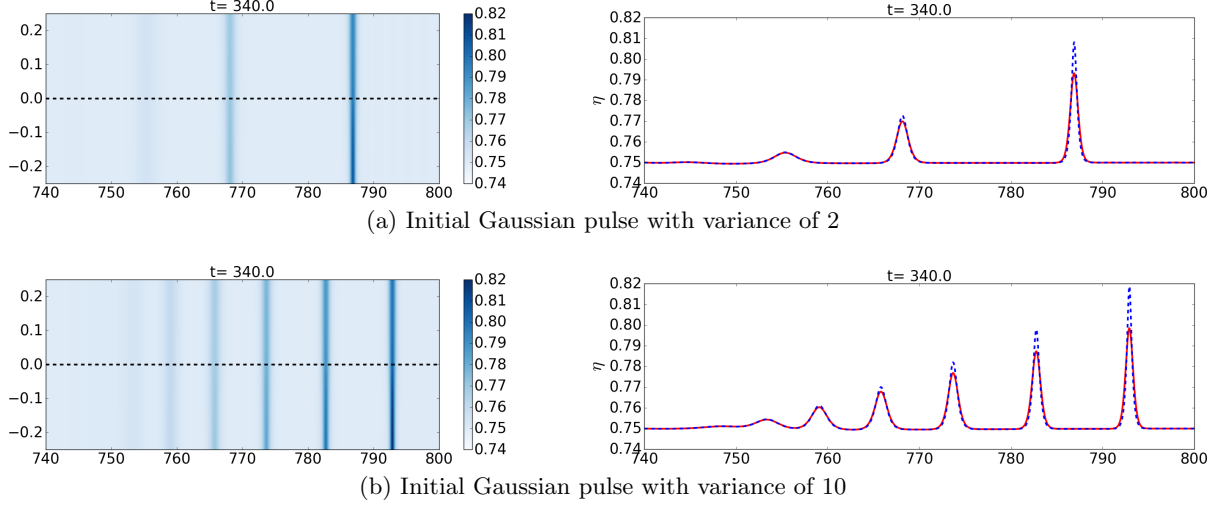(b) Initial Gaussian pulse with variance of 10

Figure 5: SW diffractons at $t = 340$. The initial condition is given by (6) with $\epsilon = 0.05$, $\eta_0 = 0.75$ and (a) $\sigma^2 = 2$ and (b) $\sigma^2 = 10$. In the left panels we show the surface plots (where the dashed line represents the location of the jump in the bathymetry) and in the right panels we show slices along the walls of the channel at $y = 0.25$ (in dashed blue) and $y = -0.25$ (in solid red).

location of the SW diffracton's peak at time t; we compute

$$D = \max_t \left[\frac{||\eta(x - X(0), y, t = 0) - \eta(x - X(t), y, t)||_{2(x,y)}}{||\eta(x - X(0), y, t = 0)||_{2(x,y)}} \right], \tag{8}$$

which represents the maximum relative difference between the solution (re-centered) at time t and the initial condition. We perform this experiment on a grid with $\Delta x = \Delta y = 1/64$ and and obtain $D \approx 3.23 \times 10^{-4}$. Afterwards, we refine the grid to $\Delta x = \Delta y = 1/128$ and and obtain $D \approx 1.46 \times 10^{-4}$. Note that we introduce a first-order error as a result of taking $X(t)$ as simply the nearest grid point to the maximum. These results indicate that SW diffractons are indeed solitary waves that propagate with a fixed shape, up to numerical errors.

3.2   Speed-amplitude and scaling relations

KdV solitons have a linear and positive speed-amplitude relation [13, 25]. This is also true for other solitary waves. For example, stegotons, which are solitary waves created due to effective dispersion introduced by reflections in periodic media, also have a linear speed-amplitude relation [15]. For the diffractons observed in [12], the relation is nonlinear (see §4.2 therein). Not surprisingly, the speed-amplitude relation for SW diffractons is also nonlinear. To demonstrate this, we isolate the first five SW diffractons from Figure 5b and propagate each by itself for a total time of $t = 100$. We plot the speed of each SW diffracton against its amplitude (starting from the mean water level η_0) in Figure 6. In addition, we show (in solid red) the linear and (in dashed black) the quadratic least-squares fitted

curves constrained to pass through the known value $c_{\text{eff}} = \sqrt{g\langle\eta_0 - b\rangle}$ for zero-amplitude waves. It is clear that the speed-amplitude relation is nonlinear.
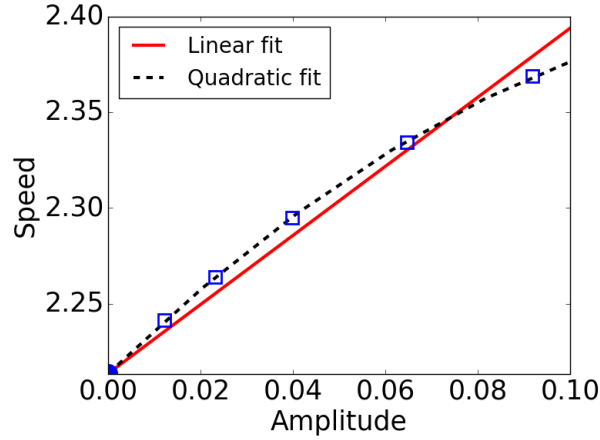

Figure 6: Speed-amplitude relation for SW diffractons. The amplitude is measured starting from the mean water level η_0. The blue squares denote measurements and the blue circle (at the origin) corresponds to $c_{\text{eff}} = \sqrt{g\langle\eta_0 - b\rangle}$, the speed of zero-amplitude waves. The solid red line and the dashed black line are linear and quadratic least-squares fitted curves constrained to pass through the point $(0, c_{\text{eff}})$.

Many solitary waves have a shape similar or identical to a sech^2 function. In addition, for some solitary waves the width varies inversely with the square root of its amplitude. We follow [12] and corroborate that this property is approximately true for SW diffractons. To see this we consider again the first four SW diffractons in Figure 5b, extract a slice along $y = 0.25$ and scale the water elevation as follows

$$\hat{\eta}(\hat{x}) := \frac{1}{A}\left[\eta\left(\hat{x}, y = 0.25\right) - \eta_0\right], \tag{9}$$

where $A = \max_x (\eta(x, y = 0.25) - \eta_0)$ and $\hat{x} = \sqrt{A}(x - x_m)$, with $x_m = \text{argmax}_x (\eta(x, y = 0.25) - \eta_0)$. In the left panel of Figure 7 we show the four non-scaled SW diffractons and in the right panel we show the same SW diffractons after the scaling defined by (9). The dashed line in the right panel is a sech^2 function with amplitude and width fitted (in a least squares sense) to the data.

3.3 Interaction of shallow water diffractons

Another well-known property of many solitary waves is their tendency to interact with one another only through a phase shift. In this section we study the interaction of two SW diffractons that are propagating in either the same direction or opposite directions. In both situations, the solitary waves are taken from the results shown in Figure 5a. In all plots we show slices of the surface elevation along the channel walls $y = 0.25$ and $y = -0.25$.
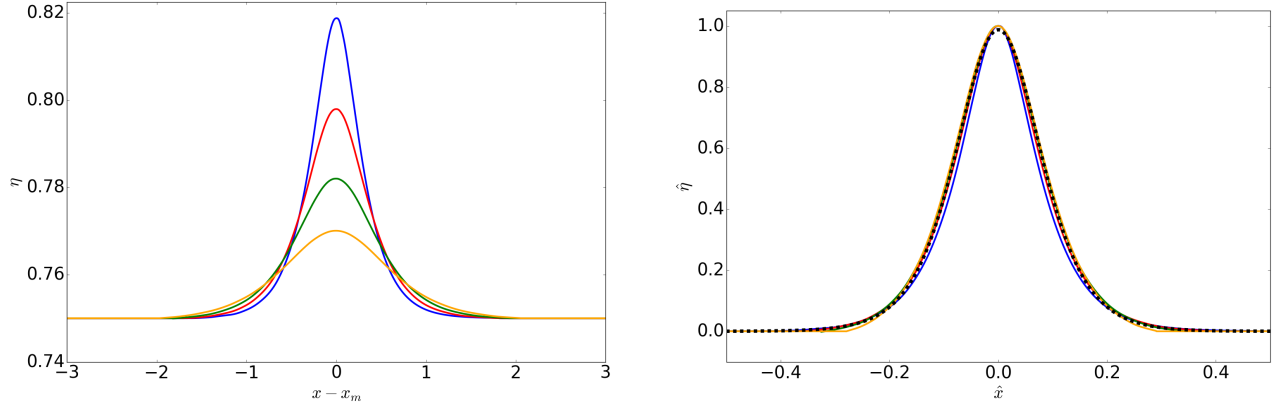
8

Figure 7: Scaling relation for SW diffractons. In the left panel we show the first four SW diffractons from Figure 5b centered at the origin. In the right panel we show the same SW diffractons after the scaling given by (9). The dashed line in the right panel is a sech^2 function fitted to the data.

To produce a counter-propagating collision we negate the velocity of the shorter SW diffracton. The initial condition is shown in the top-left panel of Figure 8. Here the taller SW diffracton propagates to the right while the smaller one moves to the left. We show the solution at different times during and after the interaction. As a reference, we propagate the taller SW diffracton by itself and superimpose the solution using dashed lines. After the interaction small oscillations are visible (see the bottom-right panel), suggesting that the interaction is not elastic. This has been reported before for diffractons [12] and other solitary waves, see for instance [2, 16, 22]. Note that there is an almost unnoticeable change in the phase for the (tallest) solitary wave with respect to the propagation without interaction; this is due to the relatively short time of interaction.

Now we consider a collision where both SW diffractons move in the same direction. The initial condition is shown in the top-left panel of Figure 9. Here both SW diffractons move to the right. Since the tallest SW diffracton moves faster (see §3.2) it eventually reaches and passes the smaller one. Again we show the solution at different times during and after the interaction. As a reference, we propagate the tallest SW diffracton by itself and superimpose the solution using dashed lines. In this case there are no visible oscillations after the collision, suggesting an elastic collision. In contrast to the counter-propagating collision, the interaction time is larger, which leads to a noticeable shift in phase. This is a common feature for other solitary waves and for diffractons.

4   Water-wave diffractons

The computational experiments of the previous section suggest that the observed solitary waves are dynamically stable solutions of the shallow water model with periodic bathymetry. We turn now to the question of whether such waves could be observed experimentally. Two questions arise immediately:

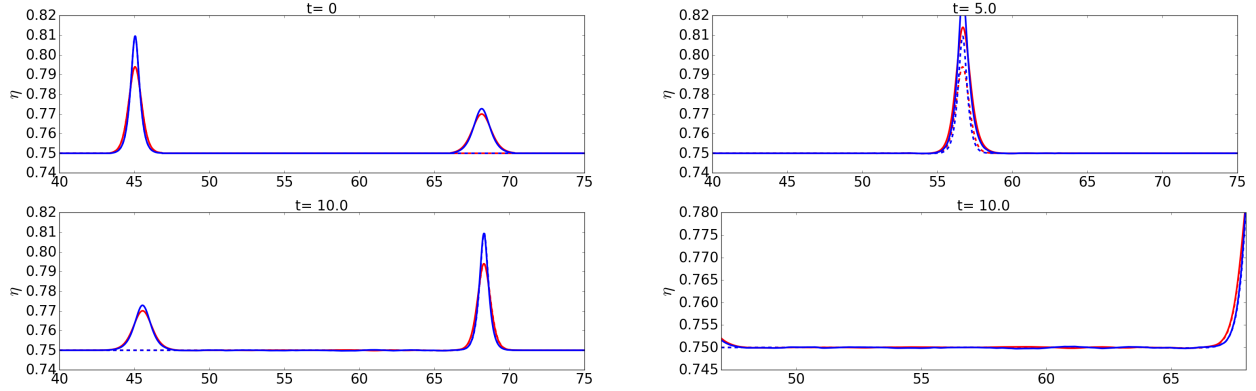1. The shallow water equations neglect the inherent dispersive nature of water waves. If solitary

Figure 8: Counter-propagating collision of SW diffractons. We show (in different color) slices at the middle of each bathymetry section. As a reference, we plot the propagation of the tallest solitary wave by itself. In the bottom-right panel we zoom to the tails of the solitary waves after the interaction to notice the oscillations.
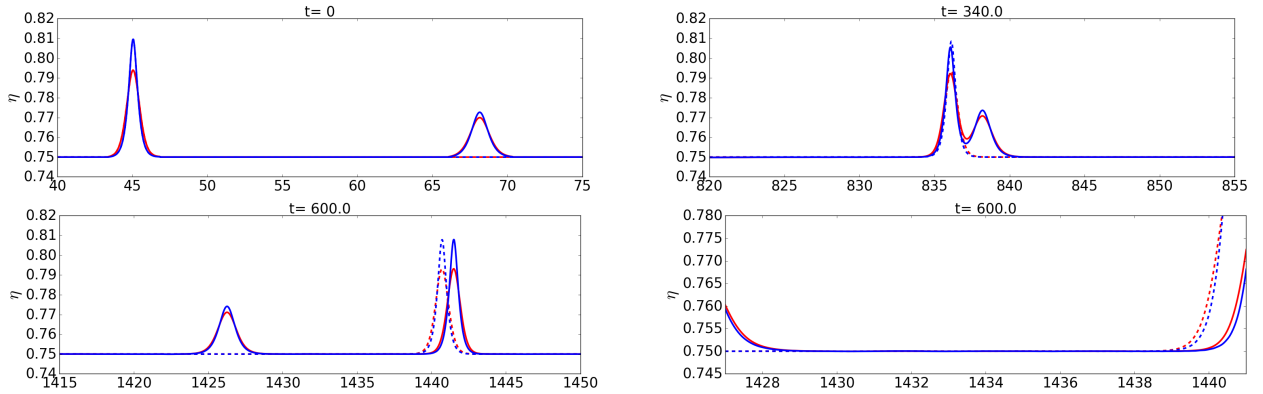

Figure 9: Co-propagating collision at different times. We show (in different color) slices at the middle of each bathymetry section. As a reference, we plot the propagation of the tallest solitary wave by itself. In the bottom-right panel we zoom to the tails of the solitary waves after the interaction.

waves over periodic bathymetry are observed experimentally, can one distinguish them from other solitary waves arising from other dispersive effects (such as those in the KdV model)?

2. The shallow water equations also neglect various dissipative effects, including viscosity, bottom friction, and surface tension. Would these effects interfere with the formation of diffractons in real water wave experiments? It is reasonable to believe that if the dissipation is too large, the formation of solitary waves might be delayed or prevented, since dissipation tends to smear steep gradients and steepening is important to the formation of solitary waves.

In §4.1 we address these two questions by making comparisons with solutions of the Korteweg-de Vries (KdV) equation. We show that it is possible to choose experimental parameters such that the bathymetric dispersion is much stronger than the dispersion present in the KdV model, so that the resulting solitary waves form before KdV solitons would. Since KdV solitons have been observed in physical experiments, this strongly suggests that dissipative effects will not prevent the formation of diffractons. To further reinforce this argument, in §4.2 we solve the full Navier-Stokes equations with variable bathymetry.

4.1 Relative strength of dispersive effects

We start by addressing the first question. To do this we consider a flat bathymetry and a weakly non-linear regime in which the (KdV) equation [13] is applicable. In this work we consider the dimensional right-going KdV equation

$$\eta_t + \sqrt{g\eta_0}\eta_x + \frac{3}{2}\sqrt{\frac{g}{\eta_0}}(\eta - \eta_0)\eta_x + \frac{1}{6}\eta_0^2\sqrt{g\eta_0}\eta_{xxx} = 0, \tag{10}$$

where as usual η is the surface elevation and η_0 is the ambient (undisturbed) surface elevation. The KdV model has been validated experimentally, for instance in [8], wherein water waves (over flat bathymetry) were observed to form solitary waves of the kind predicted by (10) after propagating over a relatively long distance. These solitary waves, which are called solitons, are created by a balance between the nonlinear effects and the dispersion in the KdV model. Soliton solutions of KdV and related equations have been studied extensively; see for instance [25]. In Figures 10a-10c we show the solution of the KdV equation (10) with initial condition given by (6) with $\epsilon = 0.025$ and $\sigma^2 = 2$. We consider three depth regimes: $\eta_0 = 0.25$, $\eta_0 = 0.5$, and $\eta_0 = 0.75$. These correspond to flow in a flat channel whose ambient depth ranges between the shallow and deep parts of the channel studied in §2 and §3. It can be seen that the relative significance of dispersion versus nonlinearity is controlled by the value of the mean depth; in deeper water dispersion dominates, while in shallower water nonlinearity becomes important and solitons start to emerge on the time scale that we consider. This behavior is already well understood but we review it here for comparison.

In Figure 10d we show the solution of the shallow water equations (3) over periodic bathymetry composed of the deep and shallow sections considered above. As predicted by the analysis and experiments in §2 and §3, effective dispersion is introduced. As a consequence, SW diffractons start to emerge on roughly the same time scale as in Figure 10c. Indeed, in these experiments, the qualitative strength and effects of the KdV dispersion and the dispersion due to periodic bathymetry are comparable.

In the following, we refer to the dispersion present in the KdV model as *KdV dispersion* and to the dispersion appearing in the shallow water model over variable bathymetry as *bathymetric dispersion*. To explore further the qualitative difference between these two sources of dispersion, we study the dispersion relations governing propagation of small-amplitude, long-wavelength waves in each model. Note that the shallow water equations under this regime can be approximated by the homogenized system (5). To obtain the dispersion relations, we assume a wave profile given by a plane wave

(a) KdV with deep flat bath. given by $\eta_0 = 0.75$

(b) KdV with flat bath. with mean average $\eta_0 = 0.5$

(c) KdV with shallow flat bath. given by $\eta_0 = 0.25$
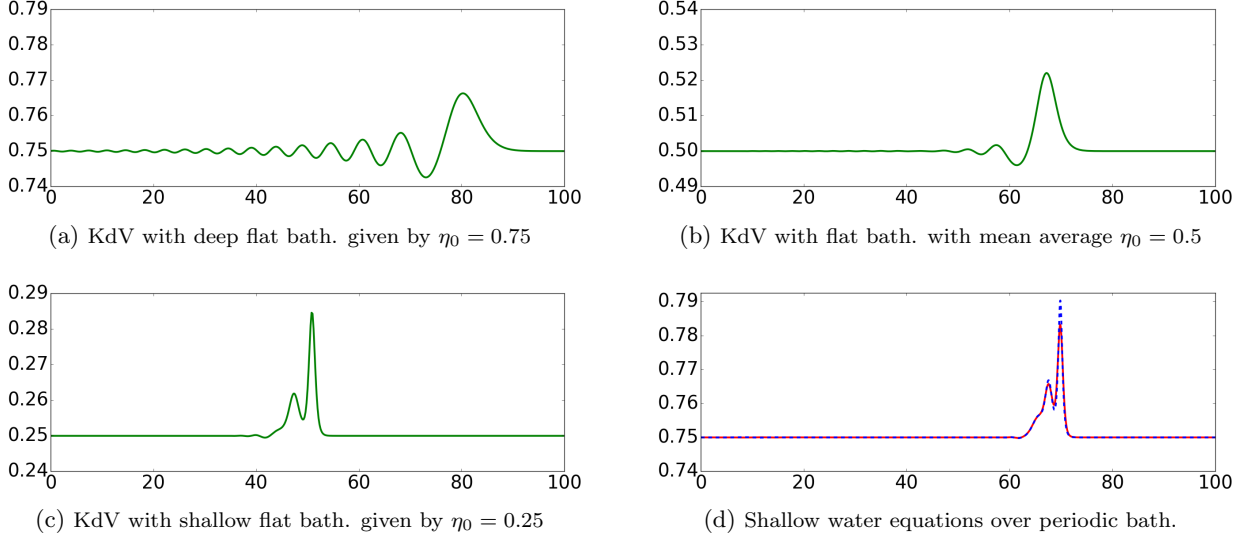

(d) Shallow water equations over periodic bath.

Figure 10: (a)-(c): solution of the KdV equation (10) at $t = 30$ for different depths given by (a) $\eta_0 = 0.75$, (b) $\eta_0 = 0.5$ and (c) $\eta_0 = 0.25$. (d): solution of the shallow water equations (3) through periodic bathymetry given by (2) with $b_A = 0$ and $b_B = 0.5$. In (d) we plot slices of the solution at $y = 0.25$ (in dashed blue) and $y = -0.25$ (in solid red).

$\eta(x, t) = \tilde{\eta}e^{i(kx - \omega t)}$, where $\tilde{\eta}$ is the amplitude, ω is the angular frequency and k is the wave number. By plugging this plane wave into a linearized version of each model, we obtain the following dispersion relations:

$$\omega_{\text{KdV}}^2 = g\bar{\eta}_0 \left(k^2 - \frac{\bar{\eta}_0^2}{3}k^4 + \frac{\bar{\eta}_0^4}{36}k^6 \right), \tag{11a}$$

$$\omega_{\text{Hom}}^2 = g\bar{\eta}_0 \left(k^2 - \alpha k^4 \right), \tag{11b}$$

for the linearized KdV and the homogenized system respectively. Here $\bar{\eta}_0$ is the mean background depth, which for KdV is simply η_0 and for the shallow water model is $\bar{\eta}_0 := \langle \eta_0 - b \rangle = \eta_0 - \frac{1}{2}(b_A + b_B)$. The linearized system on which (11b) is based is valid for low wavenumbers (see §2). Therefore, we are interested in the behavior of ω in (11) for small values of k. The leading-order (k^2) term in the two equations (which corresponds to linear, dispersionless propagation) is of course identical.

The dominant dispersive effect arises from the term of order k^4 in (11). In Figure 11 we compare the coefficient of this term in the two models, taking $\eta_0 = 0.75$ and a range of bathymetries $b_A, b_B \in [0, 0.75)$. In the figure, the red and the blue surfaces are $\frac{\bar{\eta}_0^2}{3}$ and α respectively. As one might expect, when the values of b_A and b_B are small, the bathymetric dispersion is small compared to the KdV dispersion. On the other hand, if at least one of the sections of the bathymetry is close to the mean water level, bathymetric dispersion is stronger and can be of the same order or much larger than KdV dispersion. Thus, at least for small-amplitude, long-wavelength waves, the two dispersive effects can

12

be made comparable or either one can be made dominant depending on the parameters b_A and b_B. For the parameters used in §3, the dispersion inherently present in water wave propagation would be much stronger than the dispersion introduced by diffraction. Indeed, for that particular case $\frac{\bar{\eta}_0^2/3}{\alpha} = 12$. On the other hand, it is straightforward to devise an experiment such that the dispersion due to the bathymetry is comparable or stronger than the dispersion in the KdV model. For example, if $b_A = 0$, $b_B = 0.5$ and $\eta = 0.55$, one can expect the bathymetric dispersion to be stronger. In this case, $\frac{\bar{\eta}_0^2/3}{\alpha} \approx 0.6336$. In the next section we consider further this situation.
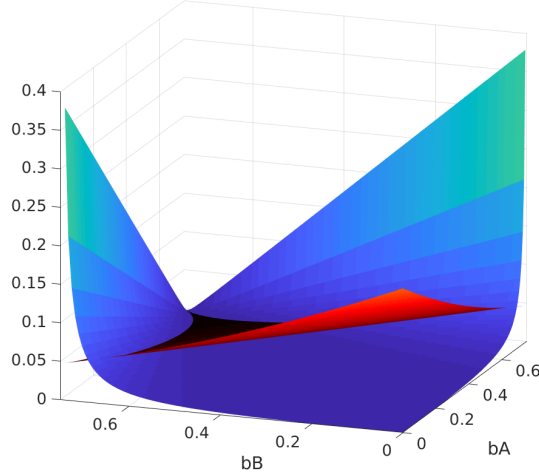

Figure 11: Coefficients of the k^4 terms in the dispersion relations (11). The red and blue curves correspond to the linearized KdV equation (10) and the homogenized system (5) respectively.

Remark 4.1.1 (About the numerical methods). *We solve the KdV equation* (10) *in a periodic domain using a pseudospectral collocation method in space and a fourth order Runge-Kutta method in time; see* [23]. *The shallow water equations and the homogenized system are solved as explained in remark* 2.2.1.

4.2 Influence of dissipation

The second question related to the feasibility of observing SW diffracton-like waves in a physical experiment is that of dissipation. As described in [25], a solitary wave starts to form when the nonlinear effects steepen the front of the wave. At this point the dispersive effects become important, introduce oscillations in the tail of the wave and prevent the formation of a shock. The oscillations grow, splitting the wave into solitary waves. If dissipative effects are dominant they might prevent steepening, delaying or even preventing the formation of solitary waves. In §4.1 we concluded that, for small amplitude waves, the dispersive effects introduced by diffraction due to changes in the

13

bathymetry can be made comparable to or dominant over the dispersion inherently present in water wave propagation. Since the dissipative effects in a physical experiment (concerning propagation of water waves) don't prevent the formation of solitons (see for instance [8]), it is reasonable to believe that SW diffracton-like water waves can also be observed. To further strengthen this argument, in this section we perform additional numerical experiments that strongly support the existence of SW diffracton-like water waves, which we call water-wave diffractons.

4.2.1   Shallow water simulations with bottom friction

We start by incorporating the effect of friction into the shallow water equations. A common model for friction is Manning's friction law which takes the form of a force term $\mathbf{f}$ on the right hand side of the shallow water equations (3) given by

$$\mathbf{f} = -\frac{gn^2||\mathbf{u}||}{h^{4/3}} \begin{bmatrix} 0 \\ hu \\ hv \end{bmatrix} \tag{12}$$

where $\mathbf{u} = [u, v]^T$ and n is Manning's friction coefficient, which is an experimental parameter with a typical value $n \approx 0.025$, see for instance [9, 14, 24]. In Figure 12 we show the solution of the shallow water model (3) with the additional friction term (12) at $t = 200$, taking a range of friction coefficients $n = 0$, 0.025, 0.033 and 0.05. The initial conditions are given by (6) with $\eta_0 = 0.75$, $\epsilon = 0.05$, and $\sigma^2 = 2$. The material parameters are given by (2) with $b_A = 0$ and $b_B = 0.5$. This setup is the same as the one in Figures 5a and 10d. In all cases SW diffractons emerge. As one might expect, the effect of friction is to delay the formation of solitary waves and to cause them to lose energy as they propagate.

4.2.2   Incompressible two-phase Navier-Stokes simulations

Finally, to incorporate the effects of fluid viscosity and surface tension, we solve the full three-dimensional incompressible Navier-Stokes equations for two-phase immiscible, viscous flows (water and air) with surface tension effects. These equations are given by

$$\rho(\partial_t \mathbf{u} + (\mathbf{u} \cdot \nabla)\mathbf{u}) - \nabla \cdot (2\mu\varepsilon(\mathbf{u})) + \nabla p = \mathbf{g}, \tag{13a}$$

$$\nabla \cdot \mathbf{u} = 0, \tag{13b}$$

where $\varepsilon(\mathbf{u}) = \frac{1}{2}\left(\nabla\mathbf{u} + \nabla\mathbf{u}^T\right)$ is the symmetric gradient, ρ and μ are the density and viscosity respectively and $\mathbf{u}$, p and $\mathbf{g}$ are the velocity, pressure and gravity fields respectively. Let Γ denote the water-air interface. The surface tension is incorporated by imposing $[\mathbf{u}]|_\Gamma = 0$ and $-[-p\mathbf{I} + 2\mu\varepsilon(\mathbf{u})]|_\Gamma \cdot \mathbf{n}^\Gamma = \gamma\kappa\mathbf{n}^\Gamma$, where $\mathbf{n}^\Gamma$ is the unit normal vector to the interface, γ is the surface tension coefficient and κ is the curvature of the interface. The physical parameters in this problem are the density and viscosity of each phase, the magnitude of the gravity field ($|\mathbf{g}|$) and the surface tension coefficient γ. These
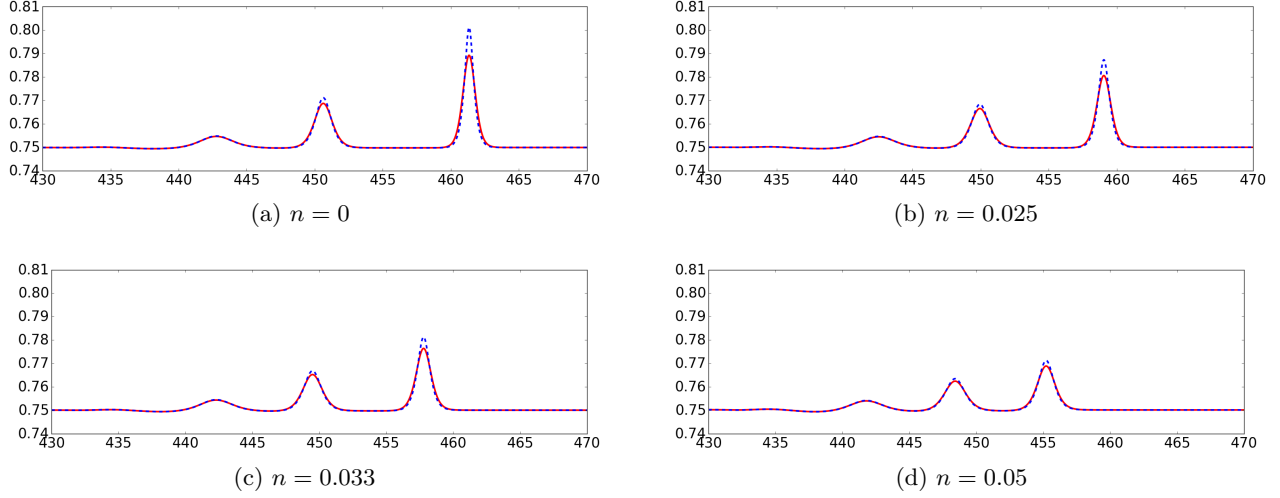
14

Figure 12: Solution of the shallow water equations (3) with Manning's friction (12) at $t = 200$. The friction coefficient is given by (a) $n = 0$, (b) $n = 0.025$, (c) $n = 033$ and (d) $n = 05$. We plot slices of the solution at $y = 0.25$ (in dashed blue) and $y = -0.25$ (in solid red).

parameters represent water and air and are given by

$$\rho_W = 998.2 \ \left(\frac{\text{kg}}{\text{m}^3}\right), \qquad \rho_A = 1.205 \ \left(\frac{\text{kg}}{\text{m}^3}\right), \qquad \mu_W/\rho_W = 1.004 \times 10^{-6} \ \left(\frac{\text{m}^2}{\text{s}}\right),$$

$$\mu_A/\rho_A = 1.5 \times 10^{-5} \ \left(\frac{\text{m}^2}{\text{s}}\right), \qquad |\mathbf{g}| = 9.8 \ \left(\frac{\text{m}}{\text{s}^2}\right), \qquad \gamma = 72.8 \times 10^{-3} \ \left(\frac{\text{kg}}{\text{s}^2}\right),$$

where W and A refer to water and air, respectively. The boundary conditions are as follows. The bottom of the water tank is set to non-slip boundary conditions, the top boundary is left open and the rest of the boundaries are set to slip boundary conditions. See remark 4.2.1 for some details about the numerical methods and remark 4.2.2 for more details about the boundary conditions.

To solve the Navier-Stokes equations over varying bathymetry requires a 3D domain, and is computationally expensive. This is pursued in §4.2.4. For comparison, we first present results of 2D simulations over a flat bottom, in §4.2.3.

4.2.3 2D simulations over a flat bottom

To validate the computational framework for these simulations and to assess the qualitative effects of the physical and numerical viscosity, we revisit the experiments over flat bathymetry in Figures 10a and 10c. This regime is expected to be properly modeled by the KdV equation (10). In Figure 13, we show in green the solution of the KdV equation at $t = 30$ and in red the water-air interface predicted by the two-phase flow Navier-Stokes solver. The agreement is good; however, the amplitude predicted

15

by the Navier-Stokes solver is smaller and the wave is slightly shifted to the left. We believe the reason for this is a combination of fluid viscosity, friction effects imposed by the non-slip boundary in the bottom of the tank and numerical viscosity. We refer to [18, §6.1.2 and §6.2.1] for further validation against experimental data.

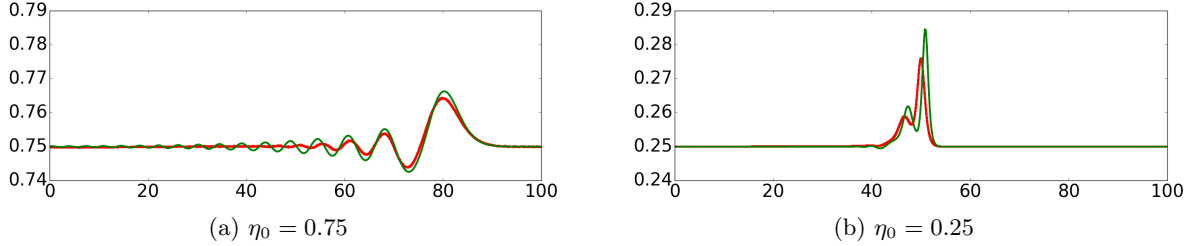(a) $\eta_0 = 0.75$ (b) $\eta_0 = 0.25$

Figure 13: In green, solution (at $t = 30$) of the KdV equation (10) and, in red, water-air interface predicted by the two-phase flow Navier-Stokes solver. The initial condition is given by (6) with $\epsilon = 0.05$, $\sigma^2 = 2$, and the indicated values of η_0. For the Navier-Stokes simulation, the initial velocity field is set to zero.

Next we present some 2D results for comparison with the 3D experiments that appear in the next section. The goal of those 3D runs is to observe solitary wave formation due to bathymetric dispersion. In order to reduce as much as possible the computational cost, we consider a regime with even stronger nonlinear and dispersive effects, which should cause solitary waves to form earlier.

For the 2D simulations, we take two initial conditions using (6) with $\epsilon = 0.35$, $\sigma^2 = 4$ and two different ambient depths given by $\eta_0 = 0.05$ and 0.55 (which correspond to the flat bathymetry profiles in the 3D experiments in the next section). The dimensions of the tank are $(x, y) \in [0, 20] \times [0, 0.9]$. Figure 14 shows the results at $t = 6$. It is clear that for the simulations with the shallower bathymetry the dispersion is not strong enough. As a result, the wave breaks strongly. Meanwhile, for the simulation with ambient depth $\eta_0 = 0.55$ the dispersive effects prevent the wave breaking; nevertheless, no solitary waves are created. We can conclude that, with flat bathymetry, nothing resembling solitary wave formation appears in any of these two experiments at the time scale of interest.
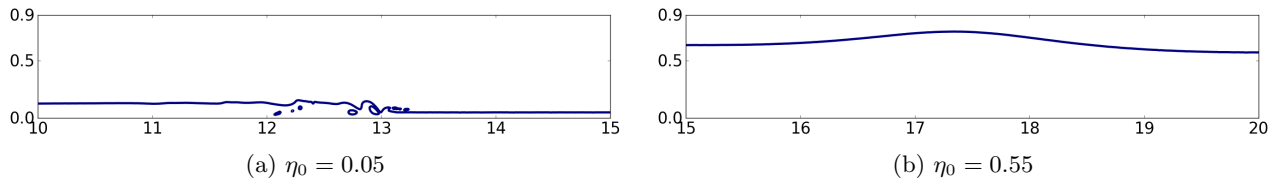

(a) $\eta_0 = 0.05$ (b) $\eta_0 = 0.55$

Figure 14: Solution at $t = 6$ of the Navier-Stokes equations (13) with the indicated ambient depth η_0. The initial wave is given by (6) with $\epsilon = 0.35$ and $\sigma^2 = 4$.
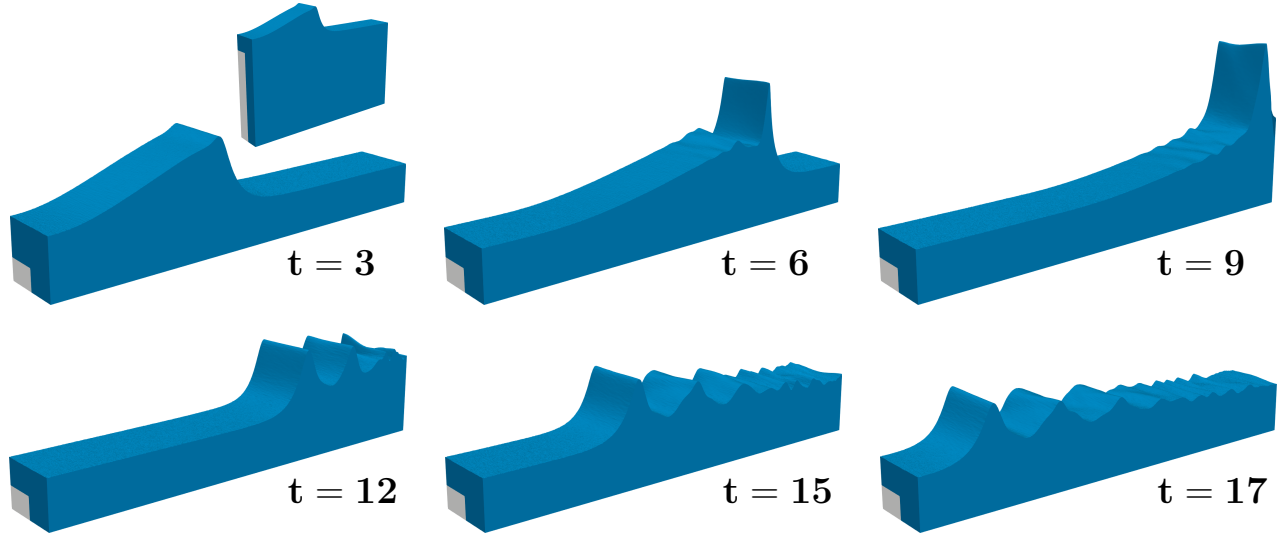
16

Figure 15: Solution of the 3D Navier-Stokes equations (13) at different times. We show the top portion of the water tank and only for the solution at $t = 3$ we insert (as a reference) a small plot of the entire domain.

4.2.4 3D simulations over variable bathymetry

Finally, we present results of a 3D Navier-Stokes simulation. The initial condition is given by (6) with $\eta_0 = 0.55$, $\epsilon = 0.35$ and $\sigma^2 = 4$. The bathymetry is given by (2) with $b_A = 0$ and $b_B = 0.5$. The dimensions of the tank are $(x, y, z) \in [0, 20] \times [-0.15, 0.15] \times [0, 1.25]$. The results at different times are shown using an isometric view in Figure 15. By $t = 6$, the initial profile already started to split into multiple peaks in a way that suggests the beginning of solitary wave formation. The front of the wave reaches the right end of the tank at around $t = 8$. After that, the wave bounces back and start to propagate to the left. As a result, the wave interacts with itself. For instance, at $t = 9$ the first solitary wave, which is propagating to the left, is superimposed with waves still traveling to the right; as a consequence, a main peak is present in the solution. However, from §3.3, we expect the solitary waves that are already forming are not dramatically affected by such interaction. Indeed, we see that at $t = 12$ the water-wave diffractons are clearly resolved.

Remark 4.2.1 (About the numerical method). *We solve the Navier-Stokes equations for two-phase immiscible viscous flows using Proteus [17] as described in [18]. This algorithm uses a phase conservative level-set method by [20] to represent and evolve the fluid interfaces and a projection scheme by [7] to solve for the incompressible Navier-Stokes equations with variable material parameters. Surface tension is incorporated following [10]. The overall algorithm is driven by a simple first-order operator splitting technique used to decouple the level-set and the Navier-Stokes stages. In all simulations we use unstructured grids with mesh size characterized by $h \approx 0.01$.*

Remark 4.2.2 (About the boundary conditions). *The boundary conditions for the velocity are summarized in Table 1. The level-set method does not require boundary conditions when the boundary is set to slip or non-slip or when the boundary is open and $\mathbf{u} \cdot \mathbf{n} \geq 0$ (where $\mathbf{u}$ is the velocity vector field and $\mathbf{n}$ is the normal unit vector to the boundary of the domain). If the boundary is open and $\mathbf{u} \cdot \mathbf{n} < 0$ we set the level-set such that only air is allowed through the boundary. We refer to [18] for more details.*

Slip		Non-slip	Open top	
$\mathbf{u} \cdot \mathbf{n} = 0,$	$[\varepsilon(\mathbf{u}) \cdot \mathbf{n}]_\tau = 0$	$\mathbf{u} = 0$	$\varepsilon(\mathbf{u}) \cdot \mathbf{n} = 0,$	$p = 0$

Table 1: Boundary conditions for the Navier-Stokes simulations.

Remark 4.2.3 (About the computational cost). *This simulation required approximately 2.5 million core-hours on the Shaheen II supercomputer[1]. The total number of (unstructured) tetrahedra is 74,482,180 which corresponds to a total of 336,447,612 degrees of freedom. The average cost to evolve one degree of freedom per time step (using one processor) was 7.63×10^{-4} seconds and the average time step size was $\Delta t = 4.83 \times 10^{-4}$ seconds.*

5 Shallow water diffractons on a channel with inclined walls

In this section we consider a channel with inclined walls like the one shown in Figure 16. This geometry is interesting since it represents a common real-world scenario. For this problem we only solve the (dispersionless) shallow water equations (3). We expect some of the behavior and conclusions from the previous sections to hold for this geometry. In particular, the dispersive effects are expected to be more significant as:

i) The change in the bathymetry increases (in this case as the inclination of the walls increases).

ii) The ambient undisturbed surface elevation is closer to the changes in bathymetry.

In Figure 17 we show the solution at $t = 200$. In the left panel we show the surface plot and in the right panel we plot a slice along $y = 0.5$.

6 Conclusions

We have shown that bathymetric variations in a channel lead to an effective dispersion that is distinct from the dispersion accounted for in wave models like KdV, and is important when the variation in bathymetry is of the same order as the overall water depth. Its presence can lead to solitary wave formation when the dominant behavior would normally be wave breaking. Although the main focus

---

[1]https://www.hpc.kaust.edu.sa/content/shaheen-ii

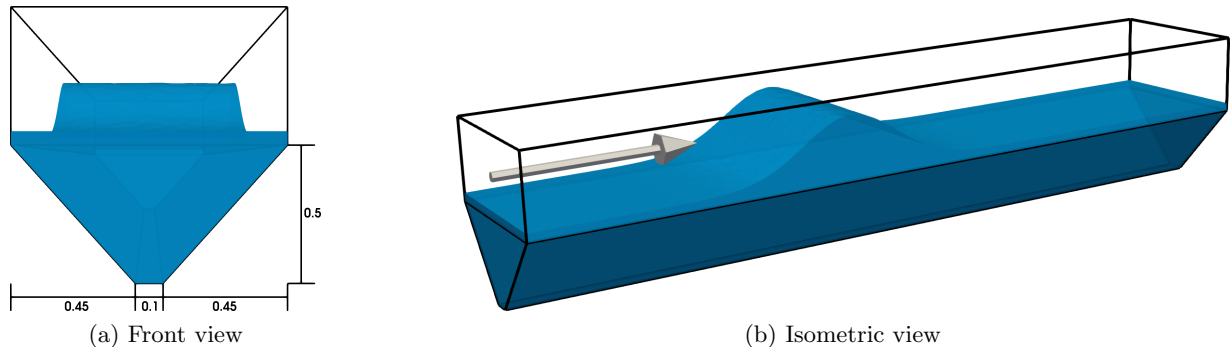(a) Front view

(b) Isometric view

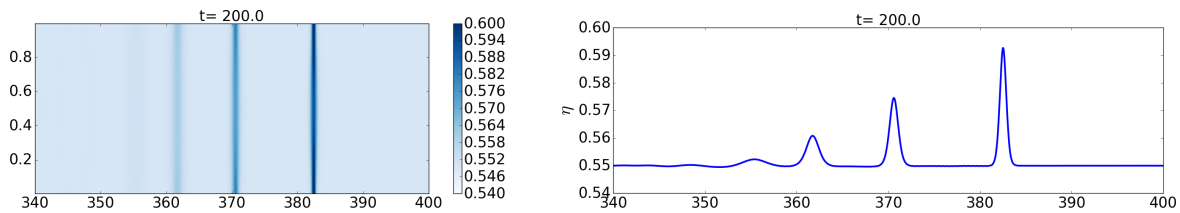Figure 16: Channel with inclined walls. The channel is infinitely long.

Figure 17: SW diffractons at $t = 200$ on a channel like the one shown in Figure 16. The initial condition is given by (6) with $\epsilon = 0.05$, $\eta_0 = 0.75$ and $\sigma^2 = 2$. In the left panel we show the surface plots and in the right panel we show slices along $y = 0.5$.

herein was on piecewise-constant bathymetry, additional simulations including those in §5 show that this phenomenon arises under a range of bathymetric profiles.

Our results suggest that experimental observation of these waves is quite feasible. Of most relevance here is the computational experiment using the 3D Navier-Stokes equations in §4.2.4. This simulation indicates that wave breaking is almost entirely avoided and an initial pulse breaks into multiple peaks, which then evolve into solitary waves. Furthermore, our experiments in §5 with a more natural channel bathymetry profile suggest that bathymetric dispersion may be important for solitary wave formation in existing real-world scenarios.

7   Acknowledgments

References

[1] J. Boussinesq. Théorie des ondes et des remous qui se propagent le long d'un canal rectangulaire horizontal, en communiquant au liquide contenu dans ce canal des vitesses sensiblement pareilles de la surface au fond. *Journal de Mathématiques Pures et Appliquées*, pages 55–108, 1872.

[2] J.G.B. Byatt-Smith. The head-on interaction of two solitary waves of unequal amplitude. *Journal of Fluid Mechanics*, 205:573–579, 1989.

[3] A.J.C. Barré de Saint-Venant. Théorie du mouvement non permanent des eaux, avec application aux crues des rivières et à l'introduction des marées dans leurs lits. *Comptes Rendus des séances de l'Académie des Sciences*, 73:237–240, 1871.

[4] Chris L Farmer, Hilary Ockendon, and John R Ockendon. Wave propagation along periodic layers. *SIAM Journal on Applied Mathematics*, 78(4):2154–2175, 2018.

[5] David L. George. Augmented riemann solvers for the shallow water equations over variable topography with steady states and inundation. *Journal of Computational Physics*, 227(6):3089 – 3113, 2008.

[6] Albert E Green and Paul M Naghdi. A derivation of equations for wave propagation in water of variable depth. *Journal of Fluid Mechanics*, 78(2):237–246, 1976.

[7] Jean-Luc Guermond and Abner Salgado. A splitting method for incompressible flows with variable density based on a pressure Poisson equation. *Journal of Computational Physics*, 228(8):2834–2846, 2009.

[8] Joseph L Hammack and Harvey Segur. The Korteweg-de Vries equation and water waves. part 2. comparison with experiments. *Journal of Fluid mechanics*, 65(2):289–314, 1974.

[9] Yuxin Huang, Ningchuan Zhang, and Yuguo Pei. Well-balanced finite volume scheme for shallow water flooding and drying over arbitrary topography. *Engineering Applications of Computational Fluid Mechanics*, 7(1):40–54, 2013.

[10] S Hysing. A new implicit surface tension implementation for interfacial flows. *International Journal for Numerical Methods in Fluids*, 51(6):659–672, 2006.

[11] David I. Ketcheson, Kyle T. Mandli, Aron J. Ahmadia, Amal Alghamdi, Manuel Quezada de Luna, Matteo Parsani, Matthew G. Knepley, and Matthew Emmett. PyClaw: Accessible, Extensible, Scalable Tools for Wave Propagation Problems. *SIAM Journal on Scientific Computing*, 34(4):C210–C231, November 2012.

[12] David I. Ketcheson and Manuel Quezada de Luna. Diffractons: Solitary waves created by diffraction in periodic media. *Multiscale Modeling & Simulation*, 13(1):440–458, 2015.

[13] Diederik Johannes Korteweg and Gustav De Vries. XLI. On the change of form of long waves advancing in a rectangular canal, and on a new type of long stationary waves. *The London, Edinburgh, and Dublin Philosophical Magazine and Journal of Science*, 39(240):422–443, 1895.

[14] Randall J LeVeque, David L George, and Marsha J Berger. Tsunami modelling with adaptively refined finite volume methods. *Acta Numerica*, 20:211–289, 2011.

[15] Randall J. LeVeque and Darryl H. Yong. Solitary waves in layered nonlinear media. *SIAM Journal on Applied Mathematics*, 63:1539–1560, 2003.

[16] Rida M Mirie and C.H. Su. Collisions between two solitary waves. Part 2. A numerical study. *Journal of Fluid Mechanics*, 115:475–492, 1982.

[17] Proteus. A finite element toolkit for computational methods and simulations, 2019. https://github.com/erdc/proteus.

[18] Manuel Quezada de Luna, J. Haydel Collins, and Christopher E. Kees. An unstructured finite element model for incompressible two-phase flow based on a monolithic conservative level set method, 2019. arXiv:1903.06919.

[19] Manuel Quezada de Luna and David I. Ketcheson. Two-dimensional wave propagation in layered periodic media. *SIAM Journal on Applied Mathematics*, 74(6):1852–1869, 2014.

[20] Manuel Quezada de Luna, Dmitri Kuzmin, and Christopher E. Kees. A monolithic conservative level set method with built-in redistancing. *Journal of Computational Physics.*, 379:262–278, 2019.

[21] F. Santosa and W. Symes. A dispersive effective medium for wave propagation in periodic composites. *SIAM Journal on Applied Mathematics*, 51:984–1005, 1991.

[22] C.H. Su and Rida M. Mirie. On head-on collisions between two solitary waves. *Journal of Fluid Mechanics*, 98(03):509–525, 1980.

[23] L.N. Trefethen. *Spectral methods in MATLAB*. Society for Industrial and Applied Mathematics, 2000.

[24] Alessandro Valiani, Valerio Caleffi, and Andrea Zanni. Case study: Malpasset dam-break simulation using a two-dimensional finite volume method. *Journal of Hydraulic Engineering*, 128(5):460–472, 2002.

[25] Norman J Zabusky and Martin D Kruskal. Interaction of "solitons" in a collisionless plasma and the recurrence of initial states. *Physical review letters*, 15(6):240, 1965.